High Efficiency Deep Blue-Emitting Organic Light Emitting Diodes based on Iridium(III) Carbene Complexes

Amlan K. Pal,[a‡] Simonas Krotkus,[b‡] Mattia Fontani,[a,c] Campbell F.R. Mackenzie,[a] David B. Cordes,[a] Alexandra M. Z. Slawin,[a] Ifor D.W. Samuel*[,b] and Eli Zysman-Colman*[,a]

[a] Organic Semiconductor Centre, EaStCHEM School of Chemistry, University of St Andrews, St Andrews, Fife, U.K., KY16 9ST, Fax: +44-1334 463808; Tel: +44-1334 463826; E-mail: eli.zysman-colman@st-andrews.ac.uk;
URL: http://www.zysman-colman.com
[b] Organic Semiconductor Centre, SUPA School of Physics and Astronomy, University of St Andrews, St Andrews, KY16 9SS Fife, U.K.
[c] Dipartimento di Chimica dell'Università degli Studi di Milano, UdR-INSTM, via Golgi 19, I-20133 Milano, Italy and SmartMatLab dell'Università degli Studi di Milano, via Golgi 19, I-20133 Milano, Italy.

‡ equal contributions

Abstract

High-efficiency pure blue phosphorescent organic light emitting diodes (OLEDs) remain one of the grand challenges principally because the emissive complexes employed either do not possess sufficiently high photoluminescence quantum yields or exhibit unsatisfactory Commission International de L'Éclairage (CIE) coordinates. Here we report two deep-blue emitting homoleptic iridium(III) complexes and demonstrate OLEDs with CIE coordinates of (0.15, 0.05) and the maximum external quantum efficiency of 13.4%, which decrease slightly to 12.5% at 100 cd m^{-2}, which represent examples of the most efficient OLEDs surpassing the CIEy requirement of the National Television System Committee (NTSC) and satisfy the most stringent blue standard for displays defined by the European Broadcasting Union (EBU). The excellent device performance is accounted for by considering

the mechanism by which the emitter orients itself in the vacuum deposited film.

Introduction:

Organic Light Emitting Diodes (OLEDs) are transforming the display and lighting industries as this technology offers the enticing combination of being extremely thin, light weight and potentially flexible with a high contrast and brightness while using low power. The emissive materials used in state-of-the-art OLEDs rely on phosphorescent complexes for red and green emitters. However, for blue emitters only fluorescent compounds are used at present as there remains a dearth of phosphorescent complexes that meet even a subset of the following criteria for deep blue emitters: (1) possess the required chromaticity standards defined by the National Television System Committee (NTSC) and European Broadcasting Union (EBU) with CIE (Commission Internationale de l'Éclairage) coordinates of (0.14, 0.08) and (0.15, 0.06), respectively; (2) possess high photoluminescence quantum yields (Φ_{PL}) that translate into high external quantum efficiencies in the OLED, particularly at useful brightnesses (at least 100 cd m^{-2} for displays and 1000 cd m^{-2} for lighting); and (3) exhibit competitive device stabilities to fluorescent complexes.[1] Of the phosphorescent complexes studied, iridium(III) compounds have attracted the widest interest as emitters in electroluminescent devices due to their high Φ_{PL}, short phosphorescence lifetimes (τ_{PL}) and facile color tunability based on the choice of ligands around the metal centre.[2] Despite these properties, the design of highly efficient pure blue phosphorescent iridium complexes remains a challenging target to achieve.[3]

In order to tune the emission to the blue, electron-withdrawing substituents are typically incorporated on the cyclometalating ligands of the iridium complexes. Three issues arise when employing this strategy. The first is that the electrochemical stability of fluoro substituents, the

most popular electron-withdrawing substituent, such as in the widely studied FIrpic [iridium(III)bis(4,6-difluopyridinato-N,$C^{2'}$)picolinate] sky blue emitter,[4] is poor, translating to greatly reduced device stability;[5] while the use of other more strongly electron-withdrawing substituents do not necessarily translate into bluer-emitting complexes, despite deepening the HOMO of the compound.[6] The second is that as the energy of the emissive triplet state increases, non-radiative recombination via thermally-accessible metal-centred excited states becomes increasingly problematic, leading to emitter degradation.[7] Finally, most iridium(III) complexes do not meet the deep blue chromaticity requirements, and instead possess CIE_y ordinates greater than 0.1 as their triplet energies are not sufficiently high (at least 2.8 eV);[3b, 8] those that do possess maximal external quantum efficiency (EQE_{max}) values <10%.[9]

Another strategy to tune the emission of charge-neutral iridium(III) complexes to the blue is to replace the coordinating pyridine rings that are typically employed with more sigma-donating heterocycles that serve to destabilize the LUMO of the complexes, such as imidazoles[10] and N-heterocyclic carbene (NHC) ligands.[9b, 10b, 11] Though iridium(III) complexes bearing arylimidazole ligands have shown high efficiencies, these emitters are not sufficiently blue[12] while most NHC-containing iridium complexes, though deep blue emitting,[13] show very low Φ_{PL}, exemplified by complexes **R1** (Φ_{PL} = 0.2% in 2-MeTHF) and **R2** (Φ_{PL} = 5% in 2-MeTHF) in Figure **1a**.[13a] With judicious design of the substituents about the cyclometalating NHC ligand, several groups have demonstrated improved efficiency OLEDs but at the expense of the deep blue nature of the emission.[14] The recent seminal work by Thompson and Forrest of *fac*/*mer*-$Ir(pmp)_3$ (pmp = [tris(*N*-phenyl,*N*-methyl-pyridoimidazol-2-yl)iridium(III)), **R3**, demonstrated that it was possible to design complexes with emission at 418 and 465 nm in 2-MeTHF and high Φ_{PL} of ca. 77%;[9b] the OLED with *fac*-$Ir(pmp)_3$ as the emitter showed CIE of (0.16, 0.09) and an External Quantum Efficiency at

1000 cd m^{-2} (EQE_{1000}) of 9.0% while that for *mer*-$Ir(pmp)_3$ as the emitter showed CIE of (0.16, 0.15) and EQE_{1000} of 13.3%. The origin of the enhanced photoluminescence quantum yield in **R3** is in part due to stabilization of the emissive triplet state and concomitant increase in the energy gap to the non-emissive metal-centred state as a function of the presence of the nitrogen atom in the pyridoimidazol-2-yl moiety, which modulates the LUMO energy.

In this study we demonstrate that high Φ_{PL} can be obtained in NHC-containing iridium complexes through sufficient stabilization of the HOMO energy, and thus the emissive triplet state, to mitigate thermal population of the non-emissive metal-centred states. We report two novel homoleptic charge-neutral meridional (*mer*-) complexes, **1** and **2** (Figure **1b**), comprising 3-methyl-1-(3/4-(trifluoromethyl)phenyl)-1*H*-3λ^4-imidazole as the pre-carbenic ligands; a structurally related complex, **R4**,[15] was recently reported as an electron blocking layer material for deep blue OLEDs. Both **1** and **2** contain the electron-withdrawing CF_3 group on the cyclometalating aryl group, the two complexes differing only in the regiochemistry of this group where in **1** the CF_3 substituent is in the more electron-withdrawing position *para* to the C-Ir bond, which is reflected in their respective Hammett parameters[16] (for CF_3**,** σ_p = 0.54, **1**; σ_m = 0.43, **2**). The difference in electron-withdrawing power is seen in both the cyclic voltammetry and DFT calculations. Both complexes showed structured, deep blue emission in dichloromethane (λ_{PL} ~ 412 nm) and as 10 wt% thin films. While **1** was moderately emissive (Φ_{PL} = 25%), the Φ_{PL} of **2** was almost three times more emissive (Φ_{PL} = 72%). The optimised OLEDs incorporating these complexes as exciton blocking (**1**) and emissive layers (**2**) show deep blue emission with CIE coordinates of (0.154, 0.052), closely matching the most stringent display requirements as set by the EBU, and EQE_{max} of 13.4%, which remains as high as 12.5% up to a display-relevant brightness of 100 cd m^{-2}. To the best of our knowledge these results

represent the best performance of the deepest-blue iridium(III)-containing OLEDs reported to date. Finally, the mechanism of the alignment of **2** during vacuum deposition is proposed, which aims to explain the high efficiencies of the OLEDs via preferential parallel alignment of the transition dipole moments resulting in an increased light outcoupling efficiency.

Results and Discussion

Iridium complexes **1** and **2**, Figure **1b**, were synthesized by reaction of NHC ligands **L1** and **L2** with $[Ir(COD)(\mu\text{-}Cl)]_2$ (where COD = 1,5-cyclooctadiene) *via* a one-pot transmetalation route using Ag_2O and triethylamine in degassed refluxing chlorobenzene (see ESI for details of synthesis).[15] A mixture of *mer*-and *fac*-homoleptic complexes were obtained and the kinetically favourable *mer*-isomer, which was the major product, could be purified by a combination of silica column chromatography and recrystallization. Complexes **1** and **2** are air- and moisture-stable off-white to colourless crystalline solids that are soluble in different organic solvents such as acetonitrile, ethyl acetate and dichloromethane. Ligands **L1**, **L2** and complexes **1** and **2** were characterized by ^{1}H, ^{13}C and ^{19}F NMR spectroscopy (see Figures **S1** and **S2** in the ESI for stacked ^{1}H NMR spectra of ligands and complexes, respectively), HRMS, melting point determination and elemental analyses. Additionally, the structures and meridional configuration of **1** and **2** were unequivocally established by single crystal X-ray diffraction analysis (Figure **1c** and Figure **S3**).

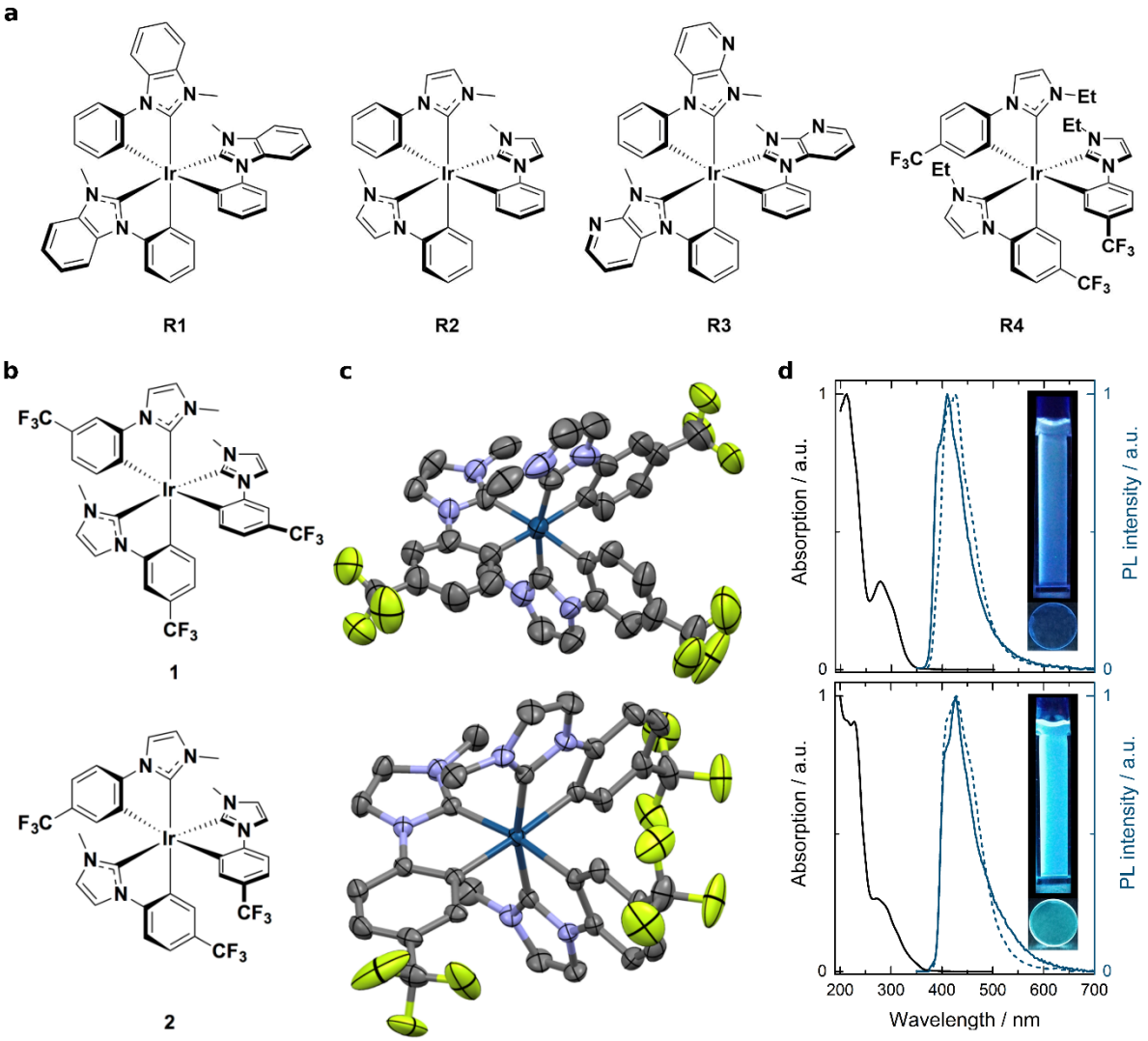

Figure **1**. **a)** Reference emissive *mer*-[Ir(C^C:)$_3$] iridium complexes R1,[13a] R2,[13a] R3[9b] and R4.[15] .**b)** Chemical structures and **c)** thermal ellipsoid plots of **1** and **2**. Only one of the independent molecules of **1** is shown. Hydrogen and solvent atoms have been omitted for clarity and ellipsoids drawn at 50 % probability. **d)** UV-Vis absorption (black line) and emission spectra (dashed blue line) in DCM and as 10 wt% PMMA doped films (solid blue line) of **1** and **2** at 298 K (λ_{exc} = 330 and 300 nm for solution and thin-film, respectively). Insets are photographic images of the solutions and thin films.

In order to elucidate the energies of the frontier molecular orbitals the electrochemical properties of **1** and **2** were investigated by cyclic voltammetry (CV) in degassed MeCN. The first redox potentials, reported with respect to SCE (Fc/Fc^+ = 0.38 V in MeCN),[17] are compiled in Table **1**, while the full set of redox potentials are detailed in Table **S3** (ESI), and the CVs are shown in Figure **S4** (ESI). Complexes **1** and **2** undergo several oxidation events, the first of which are quasi-reversible. No reduction of **1** and **2** within the accessible solvent window was observed. The oxidation potentials of **1** and **2** are anodically shifted compared to **R1**, **R2** and **R3** due to the presence of the electron-withdrawing CF_3 groups on the cyclometalating aryl ring. The cathodically shifted oxidation wave of **2** compared to **1** is in line with the shallower calculated HOMO of **2** (E_{HOMO} = -5.23 eV) versus **1** (E_{HOMO} = -5.27 eV), although DFT calculation predict a somewhat shallower HOMO for **R3** (E_{HOMO} = -5.14 eV) than what was observed experimentally.[9b] The stronger electron-withdrawing nature of the *para*-CF_3 group in **1** (*para* to Ir-C_{aryl} bond, σ_p = 0.54)[16] compared to that of the *meta*-CF_3 group in **2** (*meta* to Ir-C_{aryl} bond, σ_m = 0.43) is responsible for the 80 mV anodic shift of the first oxidation potential of **1** compared to that of **2**. DFT calculations indicate that the HOMOs of these complexes are constituted mainly of a combination of metal d-orbitals as well as the π-orbitals of cyclometalating aryl groups on the C^C ligands (Figure **3**). In the absence of any observable reduction waves for **1** and **2**, the redox gaps, ΔE_{redox}, of these complexes were inferred using the optical gaps. Complex **2** has a comparable ΔE_{redox} to **R1** while that of **1** is larger by 180 mV. The calculated LUMOs for **1** and **2** are centred predominantly on the CF_3-aryl moiety and partially on the coordinating NHC moieties, while the LUMO is localized on the pyridyl-imidazolyl (Py-Im) moiety for **R3**. The trend calculated in HOMO-LUMO energy gaps ($\Delta E_{\mathbf{1}} > \Delta E_{\mathbf{2}} > \Delta E_{\mathbf{R3}}$) match very well with the trend observed for ΔE_{redox} of these complexes.

Table **1**. Redox potentials of **1** and **2** and reference complexes **R1**, **R2** and **R3**.[a]

Cmpd	Experimental				Calculated		
	$E_{1/2}^{Ox}$ / V	$E_{1/2}^{Red}$ / V	ΔE_{redox}[b] / V	E_{HOMO} / eV[c]	E_{HOMO} / eV[d]	E_{LUMO} / eV[d]	$\Delta E_{\lvert LUMO-HOMO \rvert}$ / eV
1	0.88 (71)	----	3.70	-5.34	-5.27	-0.56	4.71
2	0.80 (90)	----	3.52	-5.27	-5.23	-0.71	4.52
R1[e]	0.76	-2.75	3.51	----	----	----	----
R2[e]	0.59	----	----	----	----	----	----
R3[f]	0.68	-2.35	3.03	----	-5.14	-1.23	3.91
R4[g]	0.74	----	3.37	-5.20	----	----	----

[a] Potentials are in volts (V) *vs*. SCE in MeCN with 0.1 M in [*n*-Bu_4N]PF_6, recorded at 298 K at a scan rate of 100 mV/s using a glassy carbon electrode as a working electrode, a platinum wire as a counter electrode and a silver wire as a reference electrode. The difference between the cathodic, E_{pc}, and anodic, E_{pa}, peak potentials, ΔE_p, (millivolts) is given in parentheses. [b] $\Delta E_{redox} = |E_{ox}-E_{red}|$. Where no reduction wave is observed, E^{red} been inferred from $E_{pa}^{ox} + E_{opt}$, where E_{opt} is taken as the energy corresponding to 10% of the intensity of the lowest energy absorption band.[18] [c] Measured orbital energies are calculated from the onset of oxidation, $E_{HOMO} = -(E_{ox}^{onset}+4.8)$ where E_{ox}^{onset} is reported *vs*. the Fc/Fc^+ couple. [d] DFT calculated orbital energies. [e] Redox potentials are from Ref [13a] in DMF, a correction factor of 0.45 V has been added to reference the data *vs*. SCE in MeCN.[19] [f] Redox potentials are from Ref [9b] in DMF, a correction factor of 0.45 V has been added to reference the data *vs*. SCE in MeCN.[19] [g] Redox potentials are from Ref [15] in DCM, a correction factor of 0.46 V has been added to reference the data *vs*. SCE.[19]

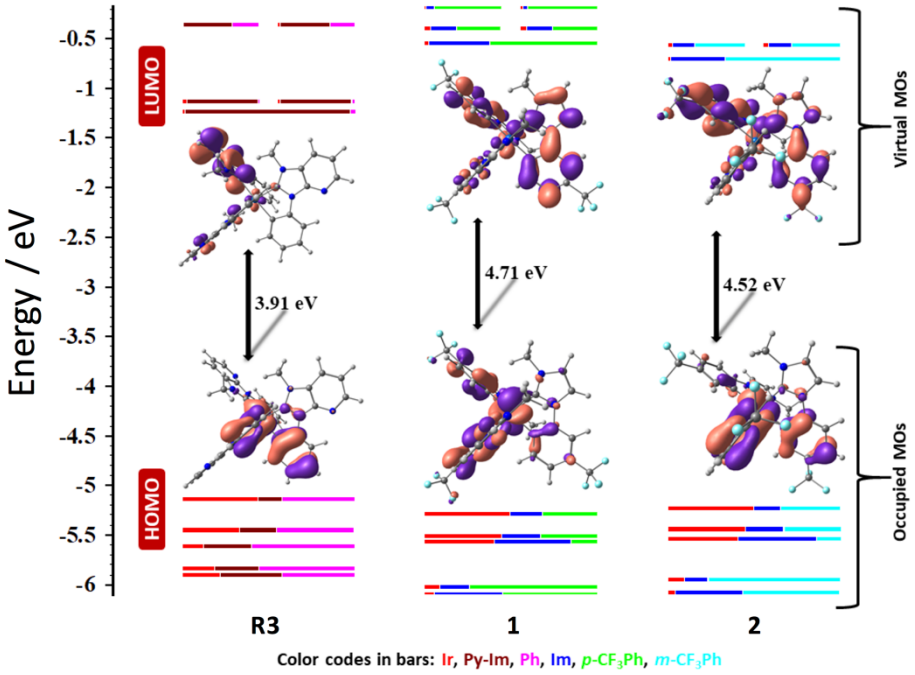

Figure **2**. Calculated frontier MO energies of **1**, **2** and **R3**, obtained from DFT [(B3LYP/SBKJC-VDZ for Ir(III)) and (6-31g**for C,H,N,(F)] with CPCM(CH_2Cl_2) and 0.5 eV threshold of degeneracy (orbitals are isocontoured at 0.03).

The UV-Vis absorption spectra of **1** and **2** were recorded in dichloromethane and the data tabulated in Table **S6** (ESI), while the spectra and overlay of the experimental spectra with the TD-DFT predicted transitions are shown in Figure **1d** and Figure **S7**, respectively. The assignment of the nature of key absorption bands are provided in Tables **S4** and **S5** (ESI). The absorption spectra of **1** and **2** show similar profiles. Absorption bands at high energy ($\lambda < 270$ nm, $\epsilon > 2.5 \times 10^4$ M^{-1} cm^{-1}) are assigned primarily to ligand centred (^{1}LC) $\pi \rightarrow \pi^*$ transitions involving both the cyclometalating aryl and carbenic imidazole moieties. For **2**, the band at 228 nm also consists of a Ir(dπ) $\rightarrow$ Imidazole(π^*) singlet mixed metal-to-ligand charge transfer (^{1}MLCT) and intra-ligand charge transfer (^{1}ILCT) transition. Bands between 270-290 nm are mixed LC and MLCT in character. The low intensity ($\epsilon \sim$ 1-1.5 $\times 10^4$ $M^{-1}cm^{-1}$) absorption maxima at 301 nm and 311 nm, respectively, for **1** and **2** are assigned principally to a mixed ^{1}MLCT/^{1}ILCT transition.[13a, 15] The observed redshift of the absorption onset at ~ 350 nm for **2** compared to that of **1** results from its smaller energy gap compared to **1** as predicted by DFT calculations. The absorption profiles of **1** and **2** are comparable to those of **R2** and **R4**; the absorption spectra of **1**, **2** and **R4** are expectedly blue-shifted compared to **R2**.

Complexes **1** and **2** show structured deep blue emission in degassed dichloromethane (Figure **1d**) that for **1** is modestly blue-shifted at 77 K in 2-MeTHF (Figure **S8**). The modestly structured emission profiles coupled with the calculated spin density distributions of **1** and **2** (Figure **S5**) suggest that the emission of these complexes originates from an admixture of triplet ligand-centred (^{3}LC) and metal-to-ligand charge transfer (^{3}MLCT) states. The energy of the triplet states of **1** and **2**, as calculated from the $E_{0\text{-}0}$ peaks at 77 K match well with their respective DFT predicted triplet state energy (E_T = 3.19 eV (77 K) and 3.42 eV (DFT) for **1** and E_T = 3.08 eV (77 K) and 3.31 eV (DFT) for **2**). While complex **1** exhibits a moderate Φ_{PL}

of 25% in solution, complex **2** is a remarkably bright emitter (Φ_{PL} = 72%), comparable to that of **R3** (Φ_{PL} = 78%) and the structurally related complex *fac*-Ir(cnpmic)$_3$ ([iridium(III)tris(1-cyanophenyl-3-methylimidazolin-2-ylidene-C,C$^{2'}$)]; Φ_{PL} = 78%),[13b] see Table **2**. Both complexes exhibit bi-exponential τ_{PL}, with longer τ_{PL} values at 77 K in deaerated 2-MeTHF in comparison to those at 298 K in degassed dichloromethane. In comparison to **R3**, the highest intensity emission maxima of **1** and **2** are significantly blue shifted (*ca.* 2079 cm^{-1} and 1914 cm^{-1} for **1** and **2**, respectively), which trends analogously to their ΔE_{redox} gaps. Compared to **R4**, complex **2** exhibits a considerably higher Φ_{PL}, likely due to a decrease in non-radiative decay *via* the shorter alkyl chain.

Complex **1** exhibits a blue-shifted emission when doped in PMMA films [PMMA = poly(methyl methacrylate)] compared to that in solution while the emission maxima do not change for complex **2** as a function of medium. However, at 77 K we observe a blue-shift for **2**, which is an indication of a greater MLCT contribution to the emissive triplet state.[13a] More importantly, the trend in relative Φ_{PL} values in solution translates similarly to those measured in the doped films where the Φ_{PL} for **2** is 46.6% compared to 13.7% for **1**.

Table **2**. Photophysical data of **1, 2** and **R1**-**R4**.

Cmpd	**In solution**				
	298 K[a]			**77 K**[b]	
	λ_{PL} / nm[c]	Φ_{PL} / %[c,d]	τ/ ns[c]	λ_{PL} / nm[c]	τ / ns[c]
1	414, 424, 453 (sh)	25	280 (65%), 1816 (35%)	388, 408, 425, 455 (sh)	1111 (79%), 2603 (21%)
2	412, 427, 454 (sh)	72	698 (48%), 1820 (52%)	402, 426, 447, 483 (sh)	1422 (73%), 3550 (27%)
R1[e]	394	0.2	15	383, 405	2400

R2[e]	~ 395[f]	5	620	384, 404, 424	2400
R3[g]	465	78	800	414	1000
R4[h]	422	32.5[i]	----	408 (sh), 422	4520

[a] In deaerated CH_2Cl_2 solution; [b] In aerated 2-MeTHF solution; [c] λ_{exc} = 330 nm (for solution measurements), 300 nm (for thin-film measurements), thin film lifetime measurements performed *in vacuo,* weighting refers to the normalised pre-exponential factors evaluated from the multi-exponential decay fit; [d] Using quinine sulfate in 0.5 M H_2SO_4, Φ_{PL} = 54.6% (for solution measurements),[20] and using an integrating sphere (for thin-film measurements); [e] From Ref [13a] in 2-MeTHF; [f] This value is not reported beyond "similar to **R1**" in Ref [13a]; [g] From Ref [9b] in 2-MeTHF; [h] From Ref [15] in THF; [i] Referenced with *fac*-Ir(ppy)$_3$ (Φ_{PL} = 100%).

In light of the attractive optoelectronic properties of complexes **1** and **2**, OLED devices were fabricated, using **2** as the emitter and **1** as an electron blocking layer (EBL). Figure **3** shows the device structures comprising **1**, **2** and various hole transport layers (HTLs). The high emission energy of **2** restricts the choice of host material. The emitting layer (EML) in all the devices consists of a DPEPO host (DPEPO = bis[2-(diphenylphosphino)phenyl]ether oxide) doped with 10 wt% of **2**. DPEPO was chosen due to its wide band gap and high triplet energy, which is higher than the triplet energy of **2** (E_T = 2.99-3.30 eV).[21] This implies that the excited state in the device is confined onto the emitter and cannot freely be transferred to the host molecules. The Φ_{PL} in the DPEPO film was 41 %. Thus, emission from the phosphorescent dopant only, along the comparatively high Φ_{PL} of up to 41% recorded in DPEPO doped films, suggest that an efficient energy transfer from DPEPO to **2** is possible (Figures **S12** and **S13**). Recorded Φ_{PL}s in the solid state show little concentration quenching up to 40 wt% dopant concentrations, likely due to the rigid molecular structure rendering molecules of **2** inert to the intermolecular interactions with the neighboring emitter molecules (Figure **S13**). The emission spectra of **2** in DPEPO were narrower and the Φ_{PL} lower compared to that observed in doped PMMA films (Figure **S12**). This can be explained by the different polarity of the surrounding host medium as well as guest-host interactions that influence the nature of the excited state. The emission lifetime of **2** embedded in the DPEPO film is 4.88 µs at room temperature (Figure **S14**) is consistent with a fast ISC rate and a ligand-centred emission originating from the lowest excited triplet state.[22] The emission lifetime is only moderately dependent on the temperature

and increases to 5.56 µs at 77 K (Figure **S15**). The decrease in the emission lifetime upon heating is consistent with the thermal population of the non-radiative state model (Figure **S15**).[23]

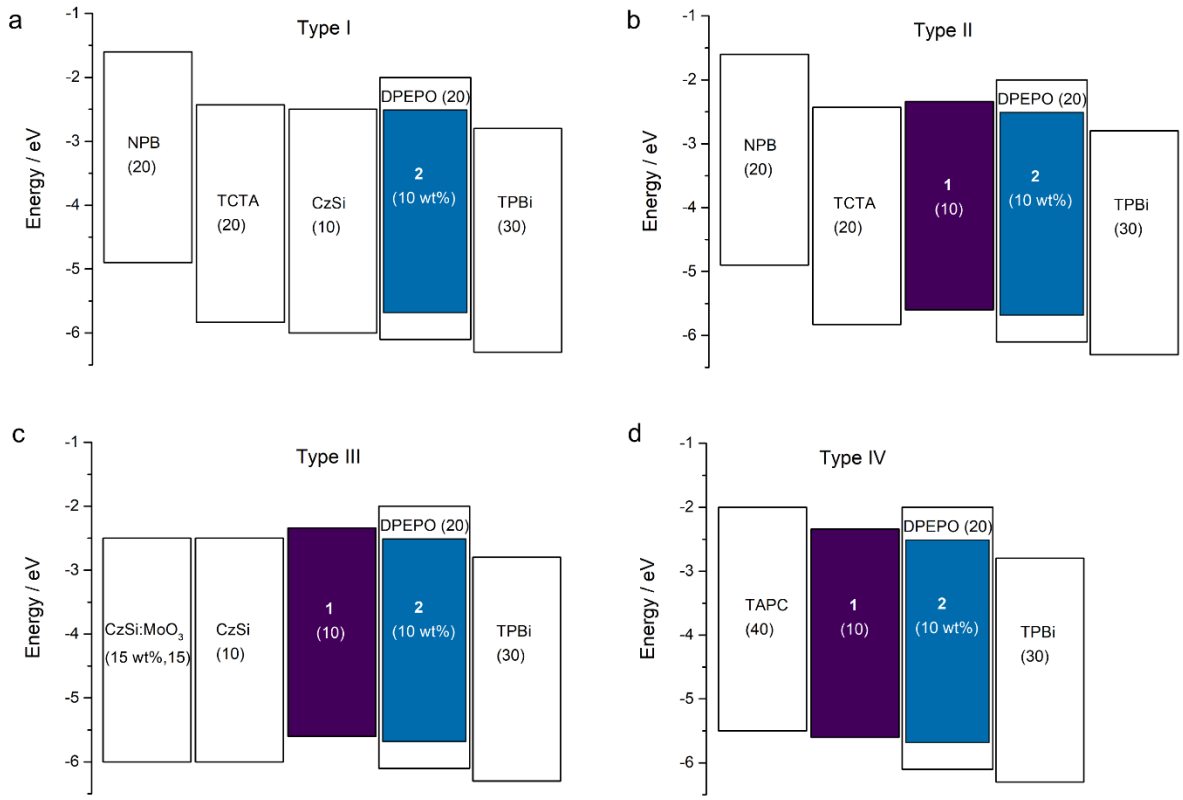

Figure **3.** Device architectures with different hole transport (HTL) and electron blocking layers (EBL). **a**) Type I device comprising NPB and TCTA as HTL. CzSi is used as a high triplet energy exciton blocker. **b**) Type II device with similar structure to Type I, but with **1** employed as an EBL. **c**, **d**, Type III and Type IV devices, consisting of CzSi and TAPC HTLs, respectively. **1** is used as an EBL and exciton blocking layer in both of these devices.

The majority of the electrons injected into the EML are transported via the host matrix before being captured by the emitter dopant and subsequently recombining with the holes trapped on the emitter molecule to form excitons. High triplet energy exciton blockers are thus needed at the HTL/EML interface to prevent non-radiative exciton recombination. The 10 nm interlayer of the high triplet energy CzSi (E_T = 3.02 eV) [CzSi = 9-(4-*tert*-butylphenyl)-3,6-bis(triphenylsilyl)-9*H*-carbazole] was therefore inserted (Type I device, Figure **3a**).[24] While **1** shows moderate Φ_{PL} in thin film, its high triplet energy and very high electronic band gap

were exploited for **1** to act as both exciton blocking and electron blocking layer in Devices II-IV, which employ different hole injection/transport layer architectures (Figure **3c-d**).

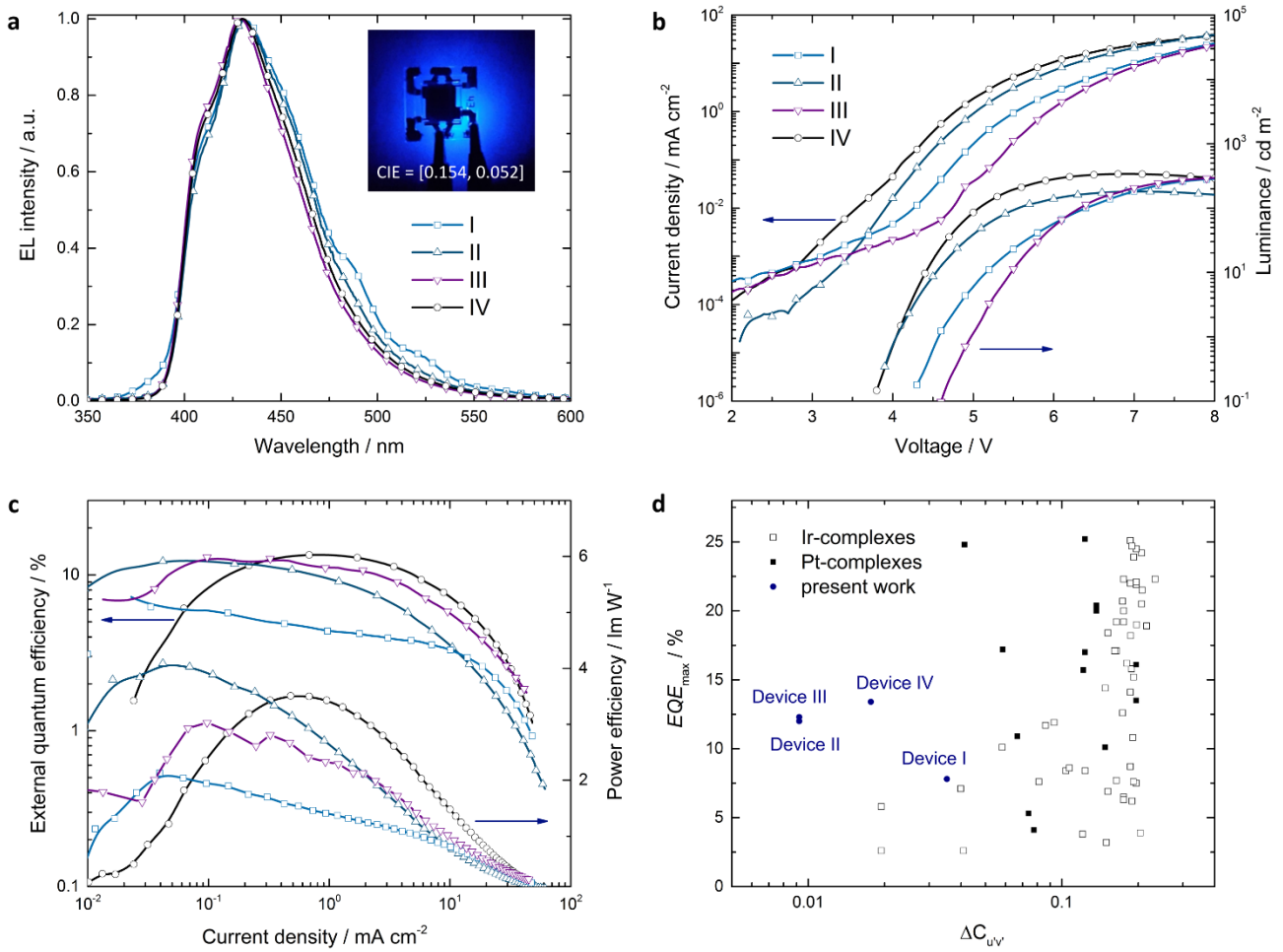

Figure **4.** Performance of deep blue phosphorescent OLEDs. **a**) Normalized electroluminescence (EL) spectra of four different OLED architectures. Inset shows the photograph of the PhOLED emission with the corresponding CIE colour coordinates of Device IV. **b**) Current density-voltage-luminance characteristics of devices I-IV. **c**) External quantum efficiency and power efficiency of PhOLEDs at different current densities. **d**) Selected peak external quantum efficiency data versus difference in CIE 1976 UCS color coordinates between OLED emission and EBU blue standard (0.15, 0.06). Data based on available literature for deep-blue OLEDs employing iridium(III) complexes (open black squares) and platinum(II) complexes (solid black squares). Solid blue circles represent results of the present work.

Figure **4** shows the performance of devices I-IV. The main device parameters are summarised in Table **3**. Deep-blue electroluminescence was recorded from all the studied PhOLEDs, with a peak emission of $\lambda_{EL} \approx 430$ nm (Figure **4a**). The role of **1** to prevent electron

leakage from the EMLs is evidenced by the lower turn-on voltage (4.05 V against 4.55 V) and an order of magnitude lower leakage current of Device II compared to Device I (Figure **4b**). The LUMO level of CzSi provides no barrier for the electrons to leave the EML. On the other hand, the shallow LUMO of **1** prevents electron leakage from the dopant molecule, as well as transports holes to the EML, which supports high charge balance within the EML and thus increases the probability of radiative exciton recombination in the DPEPO:**2** film (Figure **S16**). In addition, the difference between the triplet energy of the emitter and CzSi is shown to be not sufficient for preventing the exciton quenching at the EML/EBL interface due to thermal population of the non-radiative triplet states of the CzSi. Overall, this leads to a high maximum external quantum efficiency (EQE_{max}) of 12.1% for Device II, which corresponds to a 68% improvement compared to the moderate EQE_{max} of 7.2% of Device I (Figure **4c**). While the concept of using a wide gap phosphorescent emitter as the EBL has been demonstrated before,[9b] the use of **1** is unique because it combines very high triplet energy with a shallow LUMO, both of which are essential for achieving efficient deep blue electrophosphorescence.

The choice of the HTL sequence proved to be essential to further boost the OLED performance. Complex **1** was used in both Device III and Device IV. The selection of HTLs further shifts the high EQE values to the display-relevant brightness of 100 cd m^{-2}. The improvement in the device performance correlates with the improved charge balance at higher current densities and the lower number of the organic interfaces,[25] which is also reflected in a less red-shifted emission, as a result of suppressed polaron-induced emitter aggregation and guest or host molecular dissociation.[26] We again stress the importance of **1** in the optimal-performing device IV, as an efficient exciton/electron blocker as well as the layer that prevents exciplex formation between the HTL and the emitter, which is observed in the similar OLED without the interlayer of **1** (Figure **S17**). Optimized Device IV exhibits CIE coordinates of

(0.154, 0.052), an EQE_{max} of 13.4% and an EQE of 12.5 % at 100 cd m^{-2}, which represents to the best of our knowledge the best performance of a deep-blue OLED with color coordinates matching the display requirements for blue by the EBU. Figure **4d** shows the comparison between the Devices I-IV and reported blue phosphorescent OLEDs. The devices are compared based on the color coordinate difference in CIE1978 UCS color space between the OLED emission and the EBU standard blue colour of (0.15, 0.06). CIE1978 UCS represent the uniform chromaticity space, and thus the differences in the color coordinates represent the perceived colour difference. The device performance comparison with the selected best deep blue OLEDs is given in Table **3**.

Table **3.** Device metrics and comparison to selected literature device data with similar CIE coordinates.

Device	V_{on} / **V**	λ_{EL} / **nm**	**FWHM / nm**	**(CIE_x, CIE_y)**	***EQE* / %**		***PE* / lmW^{-1}**	
					max	**@ 100 cd m^{-2}**	**max**	**100 cd m^{-2}**
I (this work)	4.50	431	68.0	(0.154, 0.077)	7.2	3.8	2.81	1.04
II (this work)	4.05	431	65.4	(0.151, 0.059)	12.1	6.4	3.95	1.50
III (this work)	4.95	430	62.0	(0.156, 0.056)	12.3	10.0	3.00	2.00
IV (this work)	4.05	430	63.1	(0.154, 0.052)	13.4	12.5	3.50	2.98
Ref [9a], Ir emitter	-	395	-	(0.17, 0.06)	5.8	-	1.7	-
Ref [9b], Ir emitter	7.00	430	-	(0.16, 0.09)	10.1	-	-	-
Ref [27], Pt emitter		451	29	(0.148, 0.079)	24.8	22.7		
Ref [28], TADF emitter	4.00	428	65	(0.16, 0.06)	10.3	5.4	3.50	-

The impressive performance of the Device IV OLED (Figure **5a**) prompted us to investigate the contribution of light outcoupling in the device. The EQE of PhOLEDs can be expressed as $\phi_{EQE} = r_{ST}\eta_{rad}\gamma\eta_{out}$,[29] where r_{ST}, η_{rad}, γ, and η_{out} denote spin conversion factor, radiative efficiency, charge balance factor and outcoupling efficiency, respectively. Assuming

r_{ST} and γ to be close to unity,[30] $\eta_{rad} \approx 0.408$ as inferred from the Φ_{PL} measurements (Figure **S13**), and using $\eta_{EQE} = 0.134$, the extracted lower limit for the outcoupling efficiency is $\eta_{out} \approx 0.33$, which strongly deviates from the case of an isotropic emitter orientation ($\eta_{out} \approx 0.20$-0.30).[31] This discrepancy can be explained by the horizontal alignment of the transition dipole moment of the emitting species in the vacuum-deposited DPEPO:**2** film with respect to the substrate plane. In such a case, the outcoupled optical power is enhanced while the spontaneous emission rate is increased, which improves η_{out} and η_{rad}, respectively.[32] To estimate the emitter alignment, optical anisotropy of the DPEPO:**2** film was studied using variable angle spectroscopic ellipsometry (Figure **5b**). From this we extract the order parameter S=-0.26, which corresponds to a majority (84%) of transition dipole moments lying horizontal to the substrate plane.[33] Such preferential orientation of various Ir(III) organometallic complexes in thin films has been reported recently for number of emitter systems.[31b, 34] The governing mechanism responsible for the emitter alignment in the amorphous organic films is still highly debated within the scientific community. It has been proposed that the interaction between the substrate film and the impinging molecules during the evaporation process plays a key role in determining the resulting orientation in molecular glasses.[35] Jurow *et al.*[36] thus proposed that the π-π interaction between the aromatic ligands and the host molecules leads to the alignment of the aliphatic ligands (e.g., acac) towards the growth direction in heteroleptic Ir(III) complexes. On the other hand, Kim *et al.*[37] argued that Coulombic interaction between electro-positive regions of the emitter molecule and the electro-negative zones of the host enables guest-host complex formation, leading to the fixed orientation of the emitter molecules. Atomistic simulations of the deposition process were recently implemented to aid the understanding of the emitter orientation mechanism.[38] Most of the work so far, however, has been focussed on heteroleptic iridium complexes, as the inherent reduction in symmetry present in $Ir(C^N)_2(L^X)$ complexes compared to *fac*-$Ir(C^N)_3$ complexes (where C^N is a

cyclometalating ligand such as 2-phenylpyridinato and L^X is a monoanionic bidentate ancillary ligand such as acetylacetonate, acac) is expected to determine the interaction with the host molecules. While there are several experimental studies showing a net horizontal alignment of homoleptic Ir(III) complexes,[39] the mechanism by which the net orientation is achieved in this case still needs further elucidation.

Here, we propose an explanation for the observed η_{out} enhancement due to the horizonal orientation of **2** in the DPEPO host film. Figure **5c**, shows the chemical structure of the DPEPO molecule. It has a pronounced electronegative region, δ^-, which originates in part from unpaired electrons from the P=O and C-O bonds . Structurally, DPEPO is similar to another wide band gap host material for deep blue emitters, TSPO1 (TSPO1 = diphenyl[4-(triphenylsilyl)phenyl]phosphine oxide). Based on the atomistic simulations of the evaporation process, Friederich *et al.*[38c] concluded that the P=O bond in TSPO1 aligns parallel to the growth direction independent of the nature of the guest emitter molecule used and its concentration. This preferential alignment was attributed to the stabilizing van der Waals interactions between the phenyl rings of adjacent host molecules. Such P=O bond alignment was also observed recently experimentally in a structurally similar compound.[40] Following the same reasoning, we hypothesize that DPEPO molecules align in a similar fashion during deposition. The impinging emitter molecule is then exposed to a significant number of electronegative sites on the surface during the evaporation. Figure **5d** shows the calculated electrostatic potential surfaces of **1**, **2**, and reference complex **R3**, which are characterised by the high molecular asymmetry as a function of their meridional configuration, as compared to the C_3 or C_2 symmetry of the more commonly studied facial homoleptic or heteroleptic Ir(III) complexes, respectively. The molecular asymmetry manifests itself in the pronounced electropositive NHC and electronegative cyclometalating aryl ring regions within the

molecule. Therefore, in accordance with the mechanism suggested by Kim *et al.*,[37-38] we expect the emitter molecules to align with the electropositive side facing the surface, due to the electrostatic repulsion between electronegative regions in the host and phenyl rings of the C^N ligands of **2**.

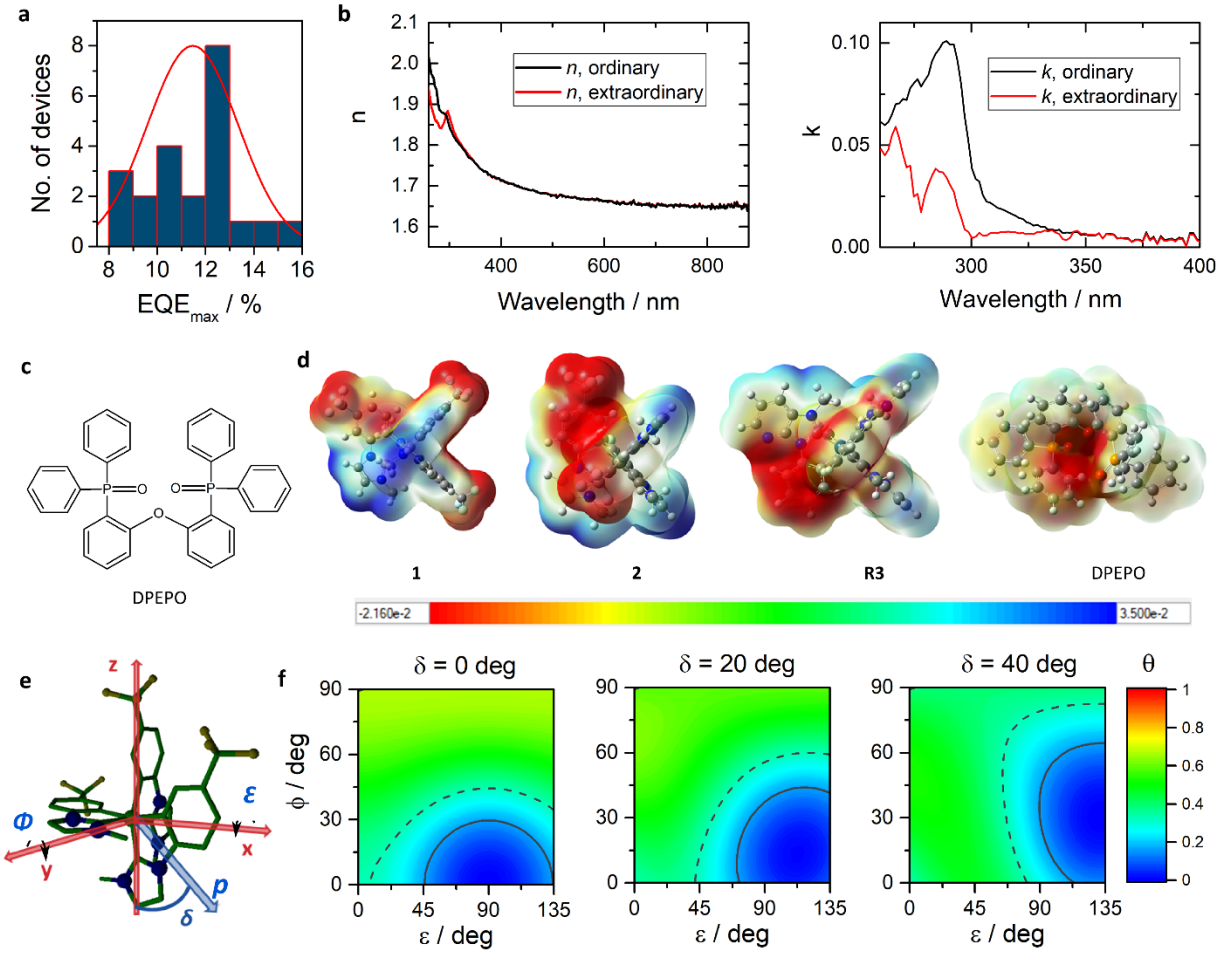

Figure **5.** Molecular orientation considerations. **a)** Statistics of Devices II-IV; **b)** optical anisotropy of DPEPO:**2** films; **c)** chemical structure of DPEPO; **d)** calculated electrostatic surface potentials of deep-blue emitting meridional Ir-NHC complexes: **1**, **2**, **R3** and the host molecule DPEPO. **e)** Definitions of the laboratory frame with respect to molecular geometry. Blue arrow shows the direction of the transition dipole moment (***p***) with respect to the molecule; the angle δ is defined between the Ir-C_{NHC} bond line and the line along ***p***; **f)** surface map of optical anisotropy factor Θ for different molecular orientations with respect to the substrate. Dashed line denotes optically isotropic films (Θ = 0.33), solid line represents expected ***p*** alignment (Θ = 0.16) of compound **2** in DPEPO host.

Having established a plausible mechanism by which the emitter molecules align during evaporation, we link the transition dipole moment orientation with respect to the laboratory

frame, following the procedure by Jurow *et al.*[36a] (Figure **5e**, see ESI for details). The molecular anisotropy factor Θ is then defined as

$$\Theta = \frac{\sum_{i=1}^{N} c_i p_{z,i}^2}{\sum_{i=1}^{N} c_i \boldsymbol{p}_i^2}$$

where $\boldsymbol{p}_i$ denotes the *i*-th transition dipole moment, $p_{z,i}$ is the corresponding component perpendicular to the substrate plane and c_i is the corresponding weighting factor. For an isotropic distribution of $\boldsymbol{p}$, Θ = 0.33 while if the $\boldsymbol{p}$ is preferentially horizontally oriented then Θ is smaller. Figure **5f** shows the calculated Θ for the meridional Ir-NHC complexes for three different angles δ between the $\boldsymbol{p}$ vector and the Ir-C_{NHC} bond axis. Typically, the transition dipole moment associated with MLCT states in iridium complexes points out from the iridium centre and lies along the ligand plane. In the case of $\boldsymbol{p}$ lying along the Ir-C_{NHC} bond axis (δ = 0°), the anisotropy factor would be close to 0.33 (Figure **5f**, dashed line) if the emitters in the vacuum deposited films indeed were oriented in a way described above, i.e. electronegative regions facing the vacuum. This situation would result in no η_{out} enhancement, contrary to the experimental evidence. Therefore, for the expected molecular orientation (ε = 135° and φ = 45°) higher δ values are required to account for the higher light extraction deduced from the device data. Combined with the data extracted from the optical anisotropy analysis, which suggests that Θ is around 0.16, we expect the δ in compound **2** to lie between 20° and 40° (Figure **5f**). As discussed by Lee *et al.*,[38b] the exact value of δ is hard to extract since the DFT calculations yield the value in a vacuum, which can vary significantly for different molecular environments. On the other hand, δ can be measured experimentally by growing emitter films in the crystalline phase. However, at such a low dopant concentration (<20 wt%) as used in the devices in this work, a crystalline phase is not formed, and the deposited guest-host films form an amorphous phase. Therefore, direct evaluation of the exact orientation of the transition dipole moment with respect to the molecular frame is not to date available.

Conclusions

In summary, two deep blue-emitting homoleptic *mer*-Ir(III) NHC complexes **1** and **2** were synthesized and comprehensively characterized. Complex **1** was used as an electron and exciton blocking layer due to its high triplet energy and shallow LUMO level while complex **2** was employed within the emitting layer in vacuum-deposited OLEDs (Devices **II, III** and **IV**) and the results compared with the device where CzSi was used as the EBL (Device **I**). A consistent improvement in EQE_{max} (7.2% to 13.4% from Device **I** to **IV**) and color purity and chromaticity (CIE_y = 0.077 to 0.052 from Device **I** to **IV**) were observed with the involvement of **1** as the electron and/or exciton blocker. The efficiency remains as high as 12.5% at the display relevant brightness of 100 cd m^{-2}. To the best of our knowledge, Device **IV** represents the bluest and best-performing iridium-based OLED reported thus far, and the only device that meets the display requirements defined by the European Broadcasting Union. The preferential parallel alignment of the transition dipole moment is shown to result in an increased outcoupled optical power, which is partially responsible for the improved performance of the OLEDs reported herein.

Acknowledgements

We are grateful to the University of St Andrews and EPSRC financial support (grants EP/P010482/1 and EP/M02105X/1). We thank Umicore AG for the gift of materials. A.K.P thanks the Leverhulme Trust Early Career Fellowship (ECF-2017-326). I.D.W.S. acknowledges a Royal Society Wolfson Research Merit award. We thank the EPSRC UK National Mass Spectrometry Facility at Swansea University for analytical services.

Supporting Information

Electronic supplementary information available: Synthetic procedure, NMR spectra, X-ray crystallographic details, electrochemistry, details of DFT calculations (including coordinates of optimised structures), luminescence studies, and OLED device fabrication and characterisation. CCDC 1852488-1852489 contains the supplementary crystallographic data for this paper. The data can be obtained free of charge from The Cambridge Crystallographic Data Centre via www.ccdc.cam.ac.uk/structures.

References

[1] X. Yang, X. Xu, G. Zhou, *J. Mater. Chem. C* **2015**, *3*, 913.

[2] A. F. Henwood, E. Zysman-Colman, *Chem. Commun.* **2017**, *53*, 807.

[3] a) Y. Chi, P.-T. Chou, *Chem. Soc. Rev.* **2010**, *39*, 638; b) Y. Im, S. Y. Byun, J. H. Kim, D. R. Lee, C. S. Oh, K. S. Yook, J. Y. Lee, *Adv. Funct. Mater.* **2017**, *27*; c) W. C. H. Choy, W. K. Chan, Y. Yuan, *Adv. Mater.* **2014**, *26*, 5368.

[4] E. Baranoff, B. F. E. Curchod, *Dalton Trans.* **2015**, *44*, 8318.

[5] V. Sivasubramaniam, F. Brodkorb, S. Hanning, H. P. Loebl, V. van Elsbergen, H. Boerner, U. Scherf, M. Kreyenschmidt, *J. Fluorine Chem.* **2009**, *130*, 640.

[6] A. K. Pal, A. F. Henwood, D. B. Cordes, A. M. Z. Slawin, I. D. W. Samuel, E. Zysman-Colman, *Inorg Chem* **2017**, *56*, 7533.

[7] a) P.-T. Chou, Y. Chi, M.-W. Chung, C.-C. Lin, *Coord. Chem. Rev.* **2011**, *255*, 2653; b) H. Fu, Y.-M. Cheng, P.-T. Chou, Y. Chi, *Mater. Today* **2011**, *14*, 472; c) Y. You, W. Nam, *Chem. Soc. Rev.* **2012**, *41*, 7061; d) D. Jacquemin, D. Escudero, *Chem Sci* **2017**, *8*, 7844.

[8] H. H. Kuo, Y. T. Chen, L. R. Devereux, C. C. Wu, M. A. Fox, C. Y. Kuei, Y. Chi, G. H. Lee, *Adv Mater* **2017**, *29*.

[9] a) R. J. Holmes, S. R. Forrest, T. Sajoto, A. Tamayo, P. I. Djurovich, M. E. Thompson, J. Brooks, Y.-J. Tung, B. W. D'Andrade, M. S. Weaver, R. C. Kwong, J. J. Brown, *Appl. Phys. Lett.* **2005**, *87*, 243507; b) J. Lee, H.-F. Chen, T. Batagoda, C. Coburn, P. I. Djurovich, M. E. Thompson, S. R. Forrest, *Nat Mater* **2016**, *15*, 92.

[10] a) U. Kazuo, S. Hisahiro, C. Cao, K. Junji, *Advanced Materials* **2014**, *26*, 5062; b) C. H. Hsieh, F. I. Wu, C. H. Fan, M. J. Huang, K. Y. Lu, P. Y. Chou, Y. H. Yang, S. H. Wu, I. C. Chen, S. H. Chou, K. T. Wong, C. H. Cheng, *Chemistry* **2011**, *17*, 9180; c) J. Zhuang, W. Li, W. Wu, M. Song, W. Su, M. Zhou, Z. Cui, *New J. Chem.* **2015**, *39*, 246; d) U. Kazuo, S. Hisahiro, I. Fumiaki, K. Junji, *Advanced Optical Materials* **2016**, *4*, 86.

[11] M. Elie, J. L. Renaud, S. Gaillard, *Polyhedron* **2018**, *140*, 158.

[12] J. Zhuang, W. Li, W. Su, Y. Liu, Q. Shen, L. Liao, M. Zhou, *Organic Electronics* **2013**, *14*, 2596.

[13] a) T. Sajoto, P. I. Djurovich, A. Tamayo, M. Yousufuddin, R. Bau, M. E. Thompson, R. J. Holmes, S. R. Forrest, *Inorganic Chemistry* **2005**, *44*, 7992; b) H. Stephan, D. C. Enrico, F. Jochen, L. J. M., L. Christian, E. Peter, F. Evelyn, M. Oliver, M. Ingo, S. Christian, W. Gerhard, *Adv. Mater.* **2008**, *20*, 3325.

[14] a) H. Sasabe, J. Takamatsu, T. Motoyama, S. Watanabe, G. Wagenblast, N. Langer, O. Molt, E. Fuchs, C. Lennartz, J. Kido, *Adv Mater* **2010**, *22*, 5003; b) Y. Cheng-Han, C. Yi-Ming, C. Yun, H. Chia-Jung, F. Fu-Chuan, W. Ken-Tsung, C. Pi-Tai, C. Chih-Hao, T. Ming-Han, W. Chung-Chih,

Angew. Chem. Int. Ed. **2007**, *46*, 2418; c) K. Y. Lu, H. H. Chou, C. H. Hsieh, Y. H. Yang, H. R. Tsai, H. Y. Tsai, L. C. Hsu, C. Y. Chen, I. C. Chen, C. H. Cheng, *Adv Mater* **2011**, *23*, 4933.

[15] Z. Chen, L. Wang, S. Su, X. Zheng, N. Zhu, C. L. Ho, S. Chen, W. Y. Wong, *ACS Appl Mater Interfaces* **2017**, *9*, 40497.

[16] C. Hansch, A. Leo, R. W. Taft, *Chem. Rev.* **1991**, *91*, 165.

[17] V. V. Pavlishchuk, A. W. Addison, *Inorg. Chim. Acta* **2000**, *298*, 97.

[18] S. Admassie, O. Inganäs, W. Mammo, E. Perzon, M. R. Andersson, *Synthetic Metals* **2006**, *156*, 614.

[19] N. G. Connelly, W. E. Geiger, *Chemical Reviews* **1996**, *96*, 877.

[20] W. H. Melhuish, *J. Phys. Chem.* **1961**, *65*, 229.

[21] a) C. Han, Y. Zhao, H. Xu, J. Chen, Z. Deng, D. Ma, Q. Li, P. Yan, *Chem. Eur. J.* **2011**, *17*, 5800; b) Q. Zhang, B. Li, S. Huang, H. Nomura, H. Tanaka, C. Adachi, *Nature Photonics* **2014**, *8*, 326.

[22] G. J. Hedley, A. Ruseckas, I. D. W. Samuel, *Chem. Phys. Lett.* **2008**, *450*, 292.

[23] T. Sajoto, P. I. Djurovich, A. B. Tamayo, J. Oxgaard, W. A. Goddard, M. E. Thompson, *Journal of the American Chemical Society* **2009**, *131*, 9813.

[24] a) M.-H. Tsai, T.-H. Ke, H.-W. Lin, C.-C. Wu, S.-F. Chiu, F.-C. Fang, Y.-L. Liao, K.-T. Wong, Y.-H. Chen, C.-I. Wu, *ACS Applied Materials & Interfaces* **2009**, *1*, 567; b) M. H. Tsai, H. W. Lin, H. C. Su, T. H. Ke, C. c. Wu, F. C. Fang, Y. L. Liao, K. T. Wong, C. I. Wu, *Adv. Mater.* **2006**, *18*, 1216.

[25] Hossein Zamani Siboni, Y. Luo, H. Aziz, *J. Appl. Phys.* **2011**, *109*, 044501.

[26] a) N. Lin, J. Qiao, L. Duan, H. Li, L. Wang, Y. Qiu, *J. Phys. Chem. C* **2012**, *116*, 19451; b) W. Qi, S. Bin, A. Hany, *Adv. Funct. Mater.* **2014**, *24*, 2975.

[27] F. Tyler, L. Guijie, W. Lele, L. Jian, *Adv. Mater.* **2014**, *26*, 7116.

[28] C.-Y. Chan, L.-S. Cui, J. U. Kim, H. Nakanotani, C. Adachi, *Adv. Funct. Mater.* **2018**, *28*, 1706023.

[29] T. Tsutsui, S. Saito, in *Intrinsically Conducting Polymers: An Emerging Technology*, 10.1007/978-94-017-1952-0_12 (Ed.: M. Aldissi), Springer Netherlands, Dordrecht, **1993**, pp. 123.

[30] M. A. Baldo, D. F. O'Brien, Y. You, A. Shoustikov, S. Sibley, M. E. Thompson, S. R. Forrest, *Nature* **1998**, *395*, 151.

[31] a) N. C. Greenham, R. H. Friend, D. D. C. Bradley, *Adv. Mater.* **1994**, *6*, 491; b) T. D. Schmidt, T. Lampe, D. Sylvinson M. R, P. I. Djurovich, M. E. Thompson, W. Brütting, *Physical Review Applied* **2017**, *8*, 037001.

[32] a) W. L. Barnes, *Journal of Modern Optics* **1998**, *45*, 661; b) K. A. Neyts, *Journal of the Optical Society of America A* **1998**, *15*, 962.

[33] D. Yokoyama, *J. Mater. Chem.* **2011**, *21*, 19187.

[34] K. H. Kim, J. J. Kim, *Adv. Mater.*, *0*, 1705600.

[35] a) S. S. Dalal, D. M. Walters, I. Lyubimov, J. J. de Pablo, M. D. Ediger, *Proc. Natl. Acad. Sci. U.S.A.* **2015**, *112*, 4227; b) M. D. Ediger, *J. Chem. Phys.* **2017**, *147*, 210901.

[36] a) M. J. Jurow, C. Mayr, T. D. Schmidt, T. Lampe, P. I. Djurovich, W. Brütting, M. E. Thompson, *Nature Materials* **2015**, *15*, 85; b) T. Lampe, T. D. Schmidt, M. J. Jurow, P. I. Djurovich, M. E. Thompson, W. Brütting, *Chem. Mater.* **2016**, *28*, 712.

[37] a) K.-H. Kim, S. Lee, C.-K. Moon, S.-Y. Kim, Y.-S. Park, J.-H. Lee, J. Woo Lee, J. Huh, Y. You, J.-J. Kim, *Nature Communications* **2014**, *5*, 4769; b) C.-K. Moon, K.-H. Kim, J. W. Lee, J.-J. Kim, *Chem. Mater.* **2015**, *27*, 2767.

[38] a) C.-K. Moon, K.-H. Kim, J.-J. Kim, *Nature Communications* **2017**, *8*, 791; b) T. Lee, B. Caron, M. Stroet, D. M. Huang, P. L. Burn, A. E. Mark, *Nano Lett.* **2017**, *17*, 6464; c) P. Friederich, R. Coehoorn, W. Wenzel, *Chem. Mater.* **2017**, *29*, 9528.

[39] a) A. Graf, P. Liehm, C. Murawski, S. Hofmann, K. Leo, M. C. Gather, *J. Mater. Chem. C* **2014**, *2*, 10298; b) L. Xiaoyue, Z. Juanye, Z. Zifeng, W. Liding, Y. Hannan, C. Qiaowen, J. Nan, L. Zhiwei, B. Zuqiang, L. Weiping, L. Zhenghong, H. Chunhui, *Advanced Materials* **2018**, *30*, 1705005.

[40] K. Suzuki, S. Kubo, F. Aussenac, F. Engelke, T. Fukushima, H. Kaji, *Angew. Chem. Int. Ed.* **2017**, *56*, 14842.

Graphical Abstract